3D Z_2 Topological Nodes in Nonsymmorphic Photonic Crystals: Ultrastrong Coupling and Anomalous Refraction

Hai-Xiao Wang,[1, *] Yige Chen,[2, *] Zhi Hong Hang,[1] Huanyang Chen,[1] Hae-Young Kee,[2, 3, †] and Jian-Hua Jiang[1, ‡]

[1]*College of Physics, Optoelectronics and Energy,*
& Collaborative Innovation Center of Suzhou Nano Science and Technology,
Soochow University, 1 Shizi Street, Suzhou 215006, China
[2]*Department of Physics, University of Toronto, Toronto, M5S 1A7, Canada*
[3]*Canadian Institute for Advanced Research, Toronto, Ontario, M5G 1Z8, Canada*
(Dated: November 10, 2021)

We propose to simulate 3D Dirac points and line-nodes with nontrivial Z_2 topology in nonsymmorphic all-dielectric photonic-crystals with space-time reversal symmetry, which can be realized at infrared and microwave frequencies. Double degeneracy of all Bloch states in high symmetry planes is achieved via nonsymmorphic screw symmetries despite the fundamental obstacle of no Kramers degeneracy in photonic crystals. Two orthogonal screw axes lead to 3D Z_2 Dirac points on high symmetry Brillouin zone boundary lines. On the other hand, Z_2 line-nodes emerge as protected twofold degeneracy of Bloch bands with opposite mirror parities on the $k_z = 0$ plane. The lowest frequency line-node is deterministic because of a degenerate-partner switching mechanism guaranteed by the fundamental properties of Maxwell equations and the nonsymmorphic screw symmetry. A pair of Fermi arcs with opposite chirality due to Z_2 topological Dirac points emerge below the light-line on (100) and (010) photonic-crystal-air interfaces. These robust surface states offer an unique opportunity to realize an "open cavity" with strong interaction between quantum emitters and engineered vacuum with nontrivial Berry phases — an important step toward topological states of strongly interacting bosons. Realistic calculation for resonant coupling between cavity-photons and phonons in boron nitride thin film yields ultrastrong coupling with vacuum Rabi splitting reaching to 23% of photon frequency. We also show that type-II Dirac cones have anomalous valley selective refraction: birefringence with both positive and negative refractions for one valley, while no refraction for the other.

PACS numbers: 42.70.Qs,78.67.Pt,03.65.Vf

I. INTRODUCTION

The study of topological properties of energy bands lies at the heart of frontiers of condensed matter physics, ranging from topological insulators[1, 2], topological superconductors[2], topological semimetals[3–5] and symmetry-protected topological states in strongly correlated quantum materials[6, 7]. Recent discoveries of Dirac[8–10] and Weyl semimetals[11–13] with ultrahigh mobility and other exotic properties bring those developments closer to material science and applications.

In parallel, photonics is another realm where achieving robust transport[14–17], selective waveguiding[18], and manipulation of angular momentum[19] are of central importance. These are the major challenges in photonic circuits, metamaterials, and quantum optics. Photonic topological states introduce new routes to overcome those challenges. For instance, back-scattering immune edge states of photonic quantum Hall systems are perfect solutions for robust and unidirectional waveguiding[20–24]. Recent developments on manipulation of light propagation via polarization and angular momentum request strong spin-orbit coupling and

angular-momentum–wavevector locking[19]. These properties are available from topological nodes in photonic bands[25–31]. Right at the heart of photonic topological states, there are nontrivial Berry phases and robust surface states, which offer unprecedented control of light and novel physical effects[11, 20, 21, 24, 32–36].

In this work, we propose to simulate 3D Z_2 topological Dirac points (DPs) and line-nodes in nonsymmorphic *all-dielectric* photonic crystals (PhCs) with space-time reversal symmetry. All-dielectric PhCs can be fabricated with well-controlled geometries from microwave to near-infrared frequencies. Disorder and interaction effects that complicate electronic band structures can be very weak in all-dielectric PhCs. Compared with plasmonic metamaterials or magneto-optical materials[26, 29], all-dielectric PhCs are lossless materials that preserve photonic coherence at large-scales and long-times. Future developments of topological photonics will benefit from simple all-dielectric PhCs, where photonic Z_2 topology becomes very important[28, 30].

However, the fundamental difference between photon and electron, is that photon, as a boson, does not have Kramers degeneracy. It is thus rather challenging to create Z_2 topological states in all-dielectric PhCs[28, 30]. Up till now, there are very few studies on 3D Z_2 topological states in PhCs, based on magneto-optical materials with glide symmetry[37] or point group symmetry[30]. In this work, we show that photonic Z_2 topological nodes

---
* These authors contributed equally
† hykee@physics.utoronto.ca
‡ jianhuajiang@suda.edu.cn

can be created using nonsymmorphic screw symmetries. Specifically, screw symmetries generate twofold degeneracy for all Bloch states on certain high symmetry planes of the Brillouin zone (BZ). This mechanism, similar to Kramers degeneracy in fermionic systems, leads to rich phenomena in band degeneracy. As a consequence, a number of 3D Z_2 DPs and Z_2 line-nodes are created, unveiling effective methodology toward photonic Z_2 topological states.

We found the "Fermi arcs" associated with Z_2 DPs, revealing that the surface states are a pair of mirror symmetric, helically dispersed bands with opposite chirality. These robust double-Fermi-arc surface states are readily observable in microwave experiments. We further show that part of the surface states survive on the (100) and (010) PhC-air interfaces, since they emerge below the light-line. Similar confinement of surface states associated with Z_2 line-nodes appear on the (001) PhC-air interface. Such surface states offer access to "open cavity" photonic states with nontrivial Berry phases. Placing hexagonal boron-nitride multilayers brings in *ultrastrong* light-matter interaction with vacuum Rabi splitting reaching to 23% of the optical phonon frequency, as induced by significant enhancement of electromagnetic fields at the interface. This system offers a practical route toward ultrastrong coupling regime for mid infrared frequency where the quantum nature of photon becomes significant[38–43]. In addition, this scheme opens the possibility toward simulation of quantum bosonic systems with both nontrivial Berry phases and strong interaction, where topological states of strongly interacting photons may emerge[7, 44]. Moreover, we find that type-II Z_2 DPs have anomalous valley-selective refraction, providing a path toward valley physics for Dirac photons.

II. NONSYMMORPHIC ALL-DIELECTRIC PHOTONIC CRYSTALS

To demonstrate creation of 3D Z_2 topological nodes using nonsymmorphic symmetries, we study a simple, all-dielectric PhC of which the structure is illustrated in Figs. 1(a), 1(b), and 1(c). It is a tetragonal lattice with space group of P4$_2$/mcm. In each unit cell (with lattice constant a along all three directions) there are two orthogonal dielectric blocks (painted as yellow and green in the figures) of the same shape that are embedded in the background medium. Each of them has length $l = 0.5a$, width $w = 0.2a$, and height $h = 0.5a$, separately. The centers of the blocks are at $(0, 0, 0)$ and $(0.5a, 0.5a, 0.5a)$, respectively (origin of the coordinate is defined as the center of the unit cell). The blocks have (relative) permittivity $\varepsilon_s = 24$, while the background medium has permittivity $\varepsilon_b = 2.2$. The blocks can be made of high-index materials such as tellurium (for wavelength longer than $4\,\mu$m), whereas the background material can be polymers such as PMMA.
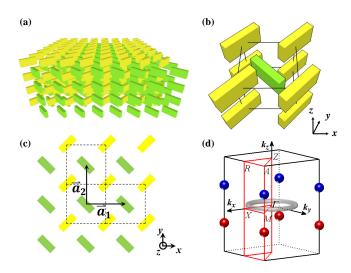

FIG. 1. (Color online) (a) Tetragonal lattice photonic crystal with nonsymmorphic symmetry. (b) Structure of a real space unit cell. The unit cell boundary is illustrated by the black lines. (c) Top-down view of the photonic crystal. Yellow and green blocks are of the same material and shape. $\vec{a}_1$ and $\vec{a}_2$ are the lattice vectors in the x-y plane. $|\vec{a}_1| = |\vec{a}_2| = a$. (d) First BZ with a pair of DPs on the M-A line and a line-node around the Γ point in the $k_z = 0$ plane. Red and blue DPs have opposite Z_2 topological charge.

The tetragonal lattice PhC possesses the following elemental symmetries,

(inversion) $\mathcal{P} : (x, y, z) \rightarrow (-x, -y, -z)$,

(glide) $G_x : (x, y, z) \rightarrow (0.5a - x, 0.5a + y, 0.5a + z)$,

(mirror) $M_1 : (x, y, z) \rightarrow (y, x, z)$,

(mirror) $M_2 : (x, y, z) \rightarrow (-y, -x, z)$. $\quad$ (1)

and their combinations. For instance, there are another glide symmetry and two screw symmetries,

$$G_y = G_x C_{2z}, \quad S_x = G_x \mathcal{P}, \quad S_y = G_y \mathcal{P}. \quad (2)$$

It is also important to define the 180° rotation along z axis

$$C_{2z} \equiv M_1 M_2 : (x, y, z) \rightarrow (-x, -y, z), \quad (3)$$

and the mirror symmetry with respect to the $z = 0$ plane,

$$M_z \equiv \mathcal{P} C_{2z} : (x, y, z) \rightarrow (x, y, -z). \quad (4)$$

The nonsymmorphic symmetries transform the yellow blocks into green blocks (and vice versa), while the symmorphic symmetries transform within each type of blocks. In PhCs, since for the same band the Bloch functions of the electric field and the magnetic field carry the same symmetry information, we will henceforth use only the magnetic fields $\vec{h}$ for the discussions on the symmetries of photonic bands. The magnetic field is a pseudovector which is even under space inversion but odd under time-reversal operation. Therefore, the explicit
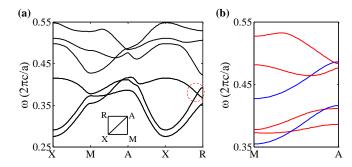
FIG. 2. (Color online) (a) Band structure for the $k_x = \frac{\pi}{a}$ plane. The dashed red circle contains an anti-crossing of two sets of doubly degenerate bands. (b) Band dispersion along the M-A line. In this line, the photonic bands are eigen functions of the C_{2z} operator. The eigenvalues can be -1 (odd parity) or 1 (even parity), as labeled by red and blue in (b), respectively. Crossing of bands with opposite parity yields DPs. Frequencies are in unit of $2\pi c/a$ with c being the speed of light in vacuum.

form of time-reversal operator for the magnetic field is $\mathcal{T} = -\mathcal{K}$ where $\mathcal{K}$ is the complex conjugation operator. Here we shall shortly denote the time-reversal operator as

$$\mathcal{T} : t \to -t. \tag{5}$$

The apparent parities (i.e., mirror symmetries) of the magnetic fields are also useful for constructing the $\vec{k} \cdot \vec{P}$ theory of photonic bands around the topological nodes [see Appendix A]. Numerical calculation in this work is largely based on the open software "MIT Photonic Bands" (see Ref. [45]). For tetragonal lattice, the spectrum and other properties remain the same if k_x and k_y are interchanged. We thus only discuss one of them in this work.

Since both time-reversal and inversion symmetry exist, the $U(1)$ Berry phase vanishes. There can only be $SU(2)$ Berry phases and Z_2 topological states. For topological nodes, there can only be Z_2 DPs and line-nodes, whereas Weyl points cannot emerge in our PhC (unless inversion symmetry is broken).

III. DIRAC POINTS AND FERMI ARC SURFACE STATES

A. Band degeneracy from screw symmetries

We now show that nonsymmorphic screw symmetries are effective tools toward doubly degenerate photonic bands. In our PhCs, the twofold degenerate bands are induced by the following *anti-unitary* symmetry opera-

tors:

$$\Theta_x \equiv S_x \mathcal{T} : (x, y, z, t) \to$$
$$(0.5a + x, 0.5a - y, 0.5a - z, -t),$$
$$\Theta_y \equiv S_y \mathcal{T} : (x, y, z, t) \to$$
$$(0.5a - x, 0.5a + y, 0.5a - z, -t), \tag{6}$$

where S_x and S_y are the screw operations defined in Eq. (2). It is straightforward to show that for all Bloch states, of the form $\Psi_{n\vec{k}}(\vec{r}) = e^{i\vec{k}\cdot\vec{r}} u_{n\vec{k}}(\vec{r})$ (u, can be a vector, is a periodic function of lattice translation, while n is the band index),

$$\Theta_x^2 \Psi_{n\vec{k}}(\vec{r}) = e^{-ik_x a} \Psi_{n\vec{k}}(\vec{r}). \tag{7}$$

The Θ_x operator transform (k_x, k_y, k_z) to $(-k_x, k_y, k_z)$. On the $k_x = \frac{\pi}{a}$ plane, which is invariant under Θ_x, one has

$$\Theta_x^2 = -1. \tag{8}$$

Therefore, all eigenstates on the $k_x = \pi/a$ plane is twofold degenerate, following similar arguments of the Kramers degeneracy in fermionic systems. Similarly, for the $k_y = \frac{\pi}{a}$ plane, *all* Bloch states are doubly degenerate due to $\Theta_y^2 = -1$. In tetragonal lattice, the spectrum is same for the $k_y = \frac{\pi}{a}$ plane as for the $k_x = \frac{\pi}{a}$ plane [shown in Fig. 2(a)]. The above results demonstrate the importance of nonsymmorphic screw symmetry in simulation of photonic Z_2 topological states.

B. Dirac Points on M-A line

DPs are fourfold degenerate points with linear-dispersion where the effective Hamiltonian describing the photonic states resembles that of massless Dirac equation [The effective Hamiltonian can be obtained via $\vec{k} \cdot \vec{P}$ expansion of the Maxwell equation around the DP (see Appendix A)]. A DP has vanishing Chern number but may carry nontrivial Z_2 topology. The topological charge of a DP can be determined by the eigenvalue of the rotation symmetry that protects the DP as shown in Ref. [46]. Z_2 topological DPs appear in pairs (at two $\vec{k}$ points linked by the time-reversal operation) with *opposite* Z_2 topological charge.

The two planes $k_x = \frac{\pi}{a}$ and $k_y = \frac{\pi}{a}$ share a common line, i.e., the M-A line: $\left(\frac{\pi}{a}, \frac{\pi}{a}, k_z\right)$, $\forall k_z$. It is crucial to notice that

$$\Theta_y \Theta_x = e^{-i(k_x + k_y)a} \Theta_x \Theta_y. \tag{9}$$

Therefore, Θ_x commutes with Θ_y on the M-A line. It makes sense that $\Theta_x \Psi_{n\vec{k}}(\vec{r})$ is the same state as $\Theta_y \Psi_{n\vec{k}}(\vec{r})$ on this line, since the Bloch states here are invariant under both M_1 and M_2 transformations. Moreover, on the M-A line C_{2z} is a symmetry operation, and

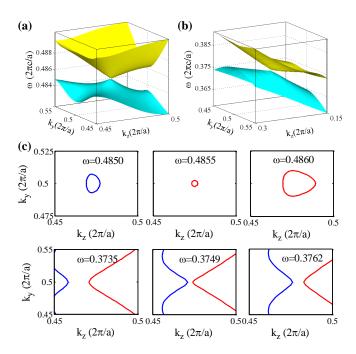$$\Theta_x \Theta_y = e^{-ik_x a} C_{2z}\big|_{k_x a = \pi} = -C_{2z}. \tag{10}$$

FIG. 3. (Color online) Photonic dispersion around a (a) type-I DP and (b) type-II DP in the k_y-k_z plane. The type-I DP is the fourth DP, while the type-II DP is the first DP, counting from low to high frequency. Isofrequency contours of the (c) type-I and (d) type-II Dirac cones.
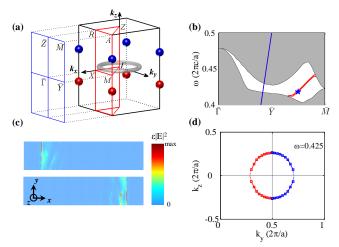

FIG. 4. (Color online) (a) DPs and surface Brillouin zone for (100) surface. Red DPs have topological charge $\mathcal{N}_{DP} = 1$, while blue ones have $\mathcal{N}_{DP} = -1$. The supercell is stacked along x direction, so that the surface BZ is projected to the k_y-k_z plane. (b) Dispersion of topological surface states (red) as well as the projected bulk photonic bands (gray). Two nearly degenerate states are labeled by a blue star. Light-line is represented by a blue line. (c) Electromagnetic energy profiles for the two surface states in the x-y plane. The wavevector of the edge states is $(0, 0.5, 0.25)\frac{2\pi}{a}$. (d) Double "Fermi arcs" due to Z_2 DPs for $\omega = 0.425(\frac{2\pi c}{a})$. The two Fermi arcs (labeled as red and blue) intersect with each other when $k_y = \pi/a$.

Thus C_{2z} commutes with both Θ_x and Θ_y. As a consequence, each doublet (i.e., $\Psi_{n\vec{k}}(\vec{r})$ and $\Theta_x\Psi_{n\vec{k}}(\vec{r})$) has the *same* C_{2z} eigenvalue (denoted as c_{2z}). Since C_{2z} is 180° rotation around z axis, its eigenvalue $c_{2z} = \pm 1$ represents parity in the x-y plane. Crossing between two sets of doublets with opposite parities yields a DP protected by the C_{2z} symmetry. The Z_2 topological charge measures parity inversion across the DP. For a DP at $(\frac{\pi}{a}, \frac{\pi}{a}, k_{DP})$, the Z_2 topological charge is given by[46]

$$\mathcal{N}_{DP} = \frac{1}{2}[c_{2z}^-(k_{DP}^+) - c_{2z}^-((k_{DP}^-)] \qquad (11)$$

where $k_{DP}^+ = k_{DP} + 0^+$ and $k_{DP}^- = k_{DP} - 0^+$ are the wavevectors slightly larger or smaller than k_{DP}, respectively. Here c_{2z}^- denotes the C_{2z} eigenvalue of the lower doublet near the DP. Therefore, a DP is a source or drain of parity inversion. For our PhCs, there are several DPs along the M-A line. The parity of those bands are labeled by colors in Fig. 2(b). We find that the lowest four DPs with $k_z > 0$ all carry topological charge $\mathcal{N}_{DP} = -1$, while the lowest four DPs with $k_z < 0$ all carry topological charge $\mathcal{N}_{DP} = 1$.

We remark that the above scenario does not apply for the X-R line ($k_x = \pi/a$ and $k_y = 0$). On these lines, according to Eq. (9), Θ_x anti-commutes with Θ_y since $k_x + k_y = \pi/a$. The degenerate partners in each doublet then have opposite c_{2z}. Hence the two sets of doubly degenerate bands can anti-cross each other, as observed in our calculation.

We notice from Fig. 2 that there are both type-I and type-II Dirac cones. To explore the properties of these DPs, we plot their dispersion on the k_y-k_z plane in Figs. 3(a) and 3(b). Fig. 3(a) shows a Dirac cone with slightly tilted dispersion (i.e., type-I), while Fig. 3(b) shows a highly tilted Dirac cone (i.e., type-II). The difference between the two Dirac cones is further displayed in Figs. 3(c) and 3(d). Here Fig. 3(c) shows that a type-I DP has closed isofrequency contours. Approaching the DP the circumference of the isofrequency contour goes to zero. In contrast, a type-II Dirac cone, as shown in Fig. 3(d), exhibits isofrequency contours consisting of two unconnected branches. In approaching the frequency of the DP, the two branches touch each other at the DP. Therefore, the density of states can be much greater for type-II DPs which may lead to enhanced light-matter interaction. We shall show in Sec. V B that type-II DPs have anomalous valley-selective refraction as well.

C. Double Fermi arc surface states on (100) surface

According to the projection principle of topological nodes[3–5, 8, 34, 47, 48], we find that the (100) and (010) surface states are associated with the Z_2 DPs. According to the symmetry of our PhC, the spectral properties of those surface states are the same. We hence focus only on the (100) surface in this section.

We calculate the edge states on the (100) surface of our photonic crystal using a supercell numerical scheme (for details, see Appendix B). The screw symmetry S_y, which is essential for double degeneracy at $k_y = \frac{\pi}{a}$, is kept for the supercell. The surface BZ is shown in Fig. 4(a). Two almost degenerate surface states can be identified in Fig. 4(b). Their field profiles in Fig. 4(c) reveal that those two states are edge states at opposite boundaries. To make sure that those are the topological edge states, we calculate the "Fermi arcs" through a scan of the edge states in the surface BZ (see Appendix B). The "Fermi arcs" for $\omega = 0.425\frac{2\pi c}{a}$ are plotted in Fig. 4(d). From the figure there are two Fermi arcs with opposite chirality (labeled as red and blue), which is significantly different from chiral Fermi arcs in Weyl PhCs[31, 34]. Those two Fermi arcs intersect with each other when $k_y = \frac{\pi}{a}$. The degeneracy of the two Fermi arcs on the $k_y = \frac{\pi}{a}$ line is protected by the Θ_y symmetry. Moreover, the spectra of the two Fermi arcs transform into each other under Θ_y which is manifested in the surface BZ as $(k_y, k_z) \rightarrow (-k_y, k_z)$. Such mirror symmetric Fermi arcs is a smoking-gun signature of the topological surface states associated with Z_2 DPs. The surface states are also found to be quite robust to surface truncation geometries (see Appendix C), demonstrating topological protection. The surface states shown here are similar to the double helicoid surface states predicted recently in an electronic material with different symmetry[48].

IV. Z_2 LINE-NODES AND THEIR SURFACE STATES

A Z_2 line-node is a line degeneracy at each point on the line there is a linear crossing through which the parity of the Bloch states is interchanged. Since a line-node is a time-reversal invariant object (it includes both a $\vec{k}$ point and its time-reversal partner $-\vec{k}$), line-nodes do not have to emerge in pairs. Line-nodes in our PhC are protected by the mirror symmetry M_z and the nonsymmorphic screw symmetries as elaborated below. The Z_2 topological charge of a line-node is defined as[49]

$$\mathcal{N}_{LN} = \frac{1}{2}(m_i - m_o). \tag{12}$$

Here m_i and m_o denote the eigenvalues of the mirror symmetry that protects the line-node for $\vec{k}$ inside and outside the line-node, respectively. They are calculated for the band with lower frequency that involves in the line-node band-crossing. $\mathcal{N}_{LN}$ can be ± 1, if the line-node is topologically nontrivial.

The line-nodes are on the $k_z = 0$ plane which is invariant under M_z. M_z commute with both Θ_x and Θ_y when $k_z = 0$. If $|m_z\rangle$ labels a Bloch state which is an eigenstate of the M_z operator with eigenvalue m_z, then

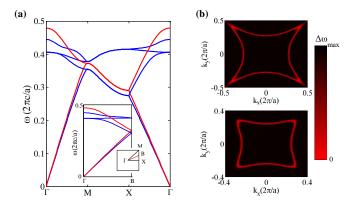$$M_z\Theta_i|m_z\rangle = \Theta_i M_z|m_z\rangle = m_z\Theta_i|m_z\rangle, \tag{13}$$

FIG. 5. (Color online) (a) Photonic band structure for $k_z = 0$ plane. Red curves label bands with $m_z = -1$, while blue curves label bands with $m_z = 1$. Inset: band structure on Γ-B line. The B point (with wavevector $(0.5, 0.25, 0)\frac{2\pi}{a}$) represents a generic, non-symmetric point on the X-M line. (b) Upper: frequency difference $\Delta\omega$ between the fourth band and the sixth band; Lower: frequency difference between the fifth band and the sixth band in the $k_z = 0$ plane. Bands are numbered according their frequencies near the Γ point in ascending orders.

for $i = x, y$. The above equation indicates that the degenerate partners, $|m_z\rangle$ and $\Theta_x|m_z\rangle$, at the X-M line has the *same* M_z eigenvalue. Due to the intrinsic property of Maxwell equations, in the long wavelength limit $\lambda \gg a$, the photonic bands become TM and TE modes which have opposite M_z eigenvalues. These two modes become degenerate in the zero frequency limit. When such degenerate bands with *opposite* M_z eigenvalues evolve to some generic point on the X-M line and then evolve back to the Γ point, there must be at least one crossing of bands with opposite M_z eigenvalues [see Fig. 5(a)]. Hence the degenerate-partner switching between bands with opposite M_z eigenvalues leads to a *deterministic* line-node. Here the lowest line-node emerge as the deterministic one. Higher line-nodes can in principle be removed by continuously tuning the photonic bands without changing the symmetry of the PhC. The lowest line-node is then protected by the mirror symmetry M_z as well as the nonsymmorphic symmetry Θ_x.

Higher line-nodes can be understood through the nature of degeneracy for higher bands at Γ point. At Γ point, all nonsymmorphic operators commute with each other as $\vec{k} = 0$. The symmetry group of Bloch states then becomes equivalent to $C_{4v} \otimes M_z$. For instance, the third and fourth bands are degenerate due to the C_{4v} group. The two bands are of the same M_z eigenvalue ($m_z = 1$) and of p-wave nature in the x-y plane. The fifth band is also of $m_z = 1$, however, it is of d-wave nature in the x-y plane and hence non-degenerate. As a consequence, there emerge another two line-nodes as the odd parity band crossing the other two even parity bands [see Fig. 5(a)]. To confirm that these crossings are indeed line-nodes, we plot the frequency difference between the
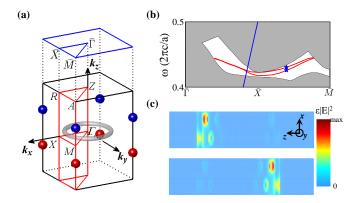
FIG. 6. (Color online) (a) Line-nodes and surface BZ for (001) surface. (b) Spectrum of the edge states (red curves) and projected bulk bands (gray regions). Two nearly degenerate surface states are labeled by two blue stars. The blue line represents the light-line. (c) Electromagnetic wave energy profiles for the two surface states in the x-z plane. The wavevectors of the two surface states are the same $(0.5, 0.2, 0)\frac{2\pi}{a}$.
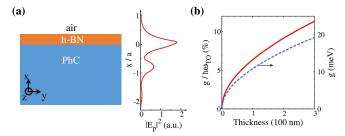

FIG. 7. (Color online) (a) Open cavity at the interface between PhC and air. Left panel: a thin film of hexagonal boron nitride is placed on top of the PhC. Right panel: distribution of intensity of inplane electric field $a^{-2}\int dy dz |E_p(\vec{r})|^2$ over the x direction. Interface between PhC and h-BN is at $x = 0$. (b) Interaction strength between TO-phonon and photon g and the ratio $g/(\hbar\omega_{TO})$. The interaction is calculated for the surface state with wavevector $\vec{k} = (0, 0.5, -0.3)\frac{2\pi}{a}$ which is in resonance with TO-phonon if $a = 3$ μm. TO-phonon has energy $\hbar\omega_{TO} = 170$ meV in h-BN.

fourth band and the sixth band, as well as that between the fifth band and the sixth band for the $k_z = 0$ plane in Fig. 5(b). Here bands are numbered according their frequencies near the Γ point in ascending order. From the figure, we confirmed that there are two higher line-nodes on the $k_z = 0$ plane, beside the deterministic line-node.

The topological charge of each line-node is defined by Eq. (12). We find that the lowest line-node is of $\mathcal{N}_{LN} = -1$, whereas the second and third line-nodes have topological charge $\mathcal{N}_{LN} = 1$. The bulk topology dictates that there are surface states on the (001) surface associated with these line-nodes. We remark that on (001) surface the Z_2 DPs have no effect, since two DPs with opposite Z_2 charge project onto the same point in surface BZ.

To reveal the topological surface states on the (001) surface, we calculate the spectrum of the surface states using a supercell with seven periods of our PhC unit cells along z direction (details are given in Appendix B). From Fig. 6(b), there are two nearly degenerate branches of surface states. Each of them is associated with one of the interface [see Fig. 6(c)]. The small splitting between them is an artifact of finite size calculation. We emphasize again that part of the surface states are below the light-line and hence can exist on the (001) PhC-air interface.

V. APPLICATIONS

A. Ultrastrong light-matter interaction at photonic-crystal–air interface

An important application of the Z_2 topological states in our PhCs is to realize an "open cavity" at the interface

between PhC and air [see Fig. 7(a)]. There are topological surface states below the light-line [see Figs. 4(b) and 6(b)]. Those surface states are confined at the PhC-air interface without additional light-trapping mechanism. We will show that such configuration is highly favorable for the study of strong light-matter interaction as well as for experimental fabrication and measurements. First, since air has lower dielectric constant than a dielectric mirror, the electric field in the air region close to the interface is much enhanced. The electric field profile in Fig. 7(a) illustrate the strong confinement of light at the PhC-air interface. Such strong light focusing can leads to very strong light-matter interaction which is crucial for the study of quantum nature of electromagnetic waves.

To demonstrate the merits of the surface states, we calculate the interaction between transverse-optical(TO)-phonon in hexagonal boron-nitride (h-BN) and cavity photon for the situation when a thin film of h-BN is placed on top of the (100) PhC-air interface. The interacting phonon-photon system is described by the following Hamiltonian,

$$H = \sum_{\vec{k}} \left[\hbar\omega_{TO}(\vec{k})b_{\vec{k}}^{\dagger}b_{\vec{k}} + \hbar\omega_{\vec{k}}a_{\vec{k}}^{\dagger}a_{\vec{k}}\right] + H_I, \quad (14a)$$

$$H_I = \sum_{\vec{k}} g_{\vec{k}}(b_{\vec{k}}^{\dagger}a_{\vec{k}} + a_{\vec{k}}^{\dagger}b_{\vec{k}}), \quad (14b)$$

where $\omega_{TO}(\vec{k})$ is the dispersion of the TO phonon which is almost flat as compared with the photonic dispersion $\omega_{\vec{k}}$ of the topological surface states. $b_{\vec{k}}^{\dagger}$ creates a TO phonon in the h-BN thin film with wavevector $\vec{k}$, whereas $a_{\vec{k}}^{\dagger}$ creates a photon in the open cavity. The collective coupling between phonon and photon is calculated as[50,

51]

$$g_{\vec{k}} = \frac{\sqrt{L_c s^2}}{2} \sqrt{\sum_l S_{u.c.}^{-1} \int_{u.c.} dy dz |E_p(y, z, x_l)|^2}, \quad (15)$$

where $L_c = 0.47$ nm is the thickness of a single h-BN monolayer, $\hbar\omega_{TO} = 170$ meV is the TO-phonon energy, the coupling coefficient is $s^2 = 3.49 \times 10^{10} (2\pi)^2 c^2 \hbar^2$ (in unit of Joule^2) as determined by experimental measurements[52]. Here $u.c.$ represents the "unit-cell" in the y-z plane, and $S_{u.c.} = a^2$ is the area of the unit cell. The integral in the above equation is performed over the strength of the electric field along the y-z plane (i.e., parallel to the h-BN monolayer plane) $|E_p|^2 = |E_y|^2 + |E_z|^2$, since polarization of the TO phonon is along the y-z plane. x_l is the position of the l-th h-BN monolayer. The electric field here is normalized as $S_{u.c.}^{-1} \int_{u.c.} d\vec{r}\epsilon(\vec{r})|\vec{E}(\vec{k}, \vec{r})|^2 = 1$ for the surface states.

The interaction g is calculated for $\vec{k} = (0, 0.5, -0.3)\frac{2\pi}{a}$. The dependence of g on the thickness of the h-BN thin film is shown in Fig. 7(b). The interaction increases approximately square root of the thickness of the thin film, since the collective coupling is proportional to the square root of number of h-BN monolayers. With a h-BN thin film of thickness 300 nm (only $0.1a$), the phonon-photon coupling g reaches to 19 meV. The vacuum Rabi splitting is as large as 23% of the phonon frequency, signifying the *ultrastrong* coupling regime[38]. We have chosen the lattice constant $a = 3$ μm to ensure that the TO-phonon is in resonance with the surface photon.

In quantum optics, when the ratio $g/\hbar\omega > 0.1$, the system enters into the ultrastrong coupling regime[39–42]. There are several nontrivial properties of an ultrastrong coupling system. For instance, the ground state of an ultrastrong coupling system has a finite population of bound photons which enables quantum vacuum emission[43]. The ultrastrong coupling system can also be exploited to study strong single photon nonlinearity and quantum phase transition[53]. Nontrivial Berry phases and strong interaction are two key elements of interacting symmetry-protected topological states, such as fractional quantum Hall states[6, 44] and bosonic topological insulators[7]. However, it is rather challenging to realize such nontrivial states in known physical systems. Our PhC open-cavity with phonon-polaritons in the ultrastrong coupling regime in mid infrared frequency might open a route to such states since both strong interaction and nontrivial Berry phases can exist in our system. Future studies should address the relevant parameter regimes for quantum simulation of strongly interacting topological phonon-polariton gas.

Furthermore, fabrication of such cavity can be much easier than the sandwich-shaped cavity as studied in the literature for both Fabry-Pérot cavities[38, 51] and PhC cavities[50]. The PhC studied here can be fabricated using mature commercial technology such as ©NanoScribe. After that the h-BN thin film can be fabricated separately and transferred to the surface. Moreover, it is easier to study the physical properties of the ultrastrong coupling phonon-photon system on the PhC-air interface. Instruments such as near field scanning can be useful for Hanbury Brown-Twiss interferometry and high-order photon correlation measurements.

B. Anomalous refraction and valley physics of type-II Z_2 Dirac Points

In our PhC, the DPs are on the M-A line with $k_x = k_y = \frac{\pi}{a}$. Through a surface 2D grating with periods along both x and y directions being $2a$, light from air can directly couple to the DPs. It is equivalent to regard the effect of the surface grating as duplicating the light cone of air at $\vec{k} = (0, 0, 0)$ to $(\frac{\pi}{a}, \frac{\pi}{a}, 0)$. The refraction of this duplicated light cone through the DPs is the focus of study in this section [see Fig. 8(a)]. We will show that type-II Z_2 Dirac cones (i.e., highly tilted Dirac cones) lead to anomalous refraction and valley physics.

In our PhC the main deformation of Dirac cones comes from a finite velocity along the z direction. Taking into account of such deformation, photonic dispersion around a DP is written as

$$\omega = \omega_0 + v(\eta q_z \pm q). \quad (16)$$

Here ω_0 is the frequency at the DP, v is the group velocity of the DP. The dimensionless parameter η measures the degree of tilt of the Dirac cone along q_z direction. Here $\vec{q} = (q_x, q_y, q_z)$ represents the deviation of the wavevector away from the DP at $(\frac{\pi}{a}, \frac{\pi}{a}, k_{DP})$ and $q = \sqrt{q_x^2 + q_y^2 + q_z^2}$.

The refraction beams are determined by the frequency ω and incident angle θ of the light. Since the dispersion is isotropic in the q_x-q_y plane, we can simplify the problem by setting $q_y = 0$. The conservation of frequency and q_x determines the angle θ' for the refraction beam,

$$\omega - \omega_0 = v(\eta q_z \pm \sqrt{q_z^2 + q_x^2}),$$
$$q_x = \frac{\omega \sin\theta}{c}, \quad \theta' \equiv -\arctan\frac{q_x}{q_z}, \quad (17)$$

where the incident angle θ is positive in our discussions. The above equations may have multiple solutions or no solution. The latter signifies no refraction through the DP, or that such a DP cannot be excited by light from air. For the case with multiple solutions, only the solutions with group velocity along z direction $v_z < 0$ delivers the refraction beam, where

$$v_z = v\left(\eta \pm \frac{q_z}{\sqrt{q_x^2 + q_z^2}}\right). \quad (18)$$

From the above equation we find that for $\eta > 1$, refraction through the DP is forbidden, since both branches have positive velocity. On the other hand, for $\eta < -1$, there are two solutions for Eq. (17) [see Fig. 8(b) for the number of refraction beams for various η and frequency
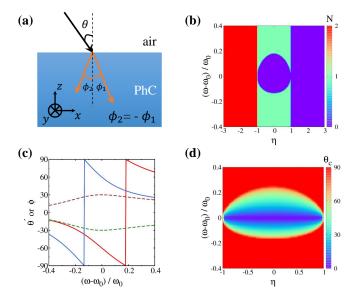
FIG. 8. (Color online) (a) Anomalous refraction of a type-II DP. A light beam from air (black arrow) is shed on the PhC, which is refracted into two beams in the PhC with different group velocities (orange arrows). The two refraction angles are always *opposite* to each other, $\phi_2 = -\phi_1$. (b) Number of refraction beams N for various frequency ω and η when the incident angle is $\theta = 50°$. There are two refraction beams for $\eta < -1$, whereas no refraction beam for $\eta > 1$. (c) The angles for the wavevectors θ' and group velocities ϕ of the two refraction beams in PhC as functions of frequency ω for incident angle $\theta = 50°$ and parameter $\eta = -2$. The red (blue) curve represents θ_1' (θ_2'), the brown (green) curve represents ϕ_1 (ϕ_2). (d) Critical angle θ_c for type-I Dirac cone vs. frequency and η. Parameters: $\omega_0 = 0.5\frac{2\pi c}{a}$ and $v = 0.2c$.

when the incident angle is $\theta = 50°$]. Indeed we observe birefringence as shown in Fig. 8(a). The two angles θ_1' and θ_2' as a function of frequency is shown in Fig. 8(c) for incident angle $\theta = 50°$, $\omega_0 = 0.5\frac{2\pi c}{a}$, and $v = 0.2c$. We notice that q_z can switch sign for both refraction beams (as indicated by abrupt change in θ'). An important quantity of the refraction beams is the group velocity, consisting of both z and x components,

$$v_x = \pm v \frac{q_x}{\sqrt{q_x^2 + q_z^2}}, \quad \phi \equiv -\arctan\frac{v_x}{v_z}. \quad (19)$$

From Fig. 8(c) we observe a rather simple relation between the two refraction beams,

$$\phi_1 = -\phi_2. \quad (20)$$

The above relation indicates that one of the refraction beam has negative refraction. The above relation emerges because for $\eta < -1$ there is a solution for each branch ($\pm$) with

$$q_{z,\pm} = \frac{\eta(\omega - \omega_0) \pm \sqrt{(\omega - \omega_0)^2 + v^2(\eta^2 - 1)q_x^2}}{v(\eta^2 - 1)}. \quad (21)$$

We emphasize that the magnitude of the two group velocity is different, unless $\omega = \omega_0$. Because DPs appear in pairs with opposite η due to time-reversal symmetry. For type-II DPs, one of the Dirac cone cannot be excited, whereas the other one exhibits birefringence. This interesting phenomenon provides a route to valley selective physics for photonic DPs. We emphasize that when light is incident from the bottom surface (instead of the top surface) of the PhC, opposite valley contrast is realized, since in this geometry the refraction beams must have $v_z > 0$.

In contrast, for type-I DPs, excitation of the Dirac cone is possible if the incident angle is smaller than a critical angle θ_c. If $\theta < \theta_c$ there is only one refraction beam. We plot θ_c for various frequency and η in Fig. 8(d). From the figure we find that the critical angle θ_c is the same for both negative and positive η with the same $|\eta|$ at the same frequency. Therefore, type-I DPs have no valley contrasting in refraction.

VI. CONCLUSIONS AND DISCUSSIONS

We propose an effective method for simulation of 3D Z_2 topological nodes in all-dielectric PhCs with space-time reversal symmetry using nonsymmorphic screw symmetries. In a concrete example we show that for a tetragonal lattice with space group of P4$_2$/mcm, the screw symmetries lead to double degeneracy in high symmetry planes in the BZ. In this way, the screw symmetries play a similar role as Kramers degeneracy for spin-1/2 electronic Z_2 topological states.

Using this method, we find a number of Z_2 DPs on the M-A line (i.e., the common line of the doubly degeneracy planes). We also find Z_2 line-nodes around the Γ point on the $k_z = 0$ plane for the first few photonic bands. The lowest line-node emerges in a deterministic manner because of a *degenerate-partner switching* mechanism: the degenerate-partners have the opposite parities at the Γ point due to TE-TM degeneracy at zero frequency but have the same parity on the boundaries of the BZ on the $k_z = 0$ plane due to nonsymmorphic screw symmetry. Hence there must be a line crossing of bands during the evolution between the Γ point and BZ boundaries.

As a consequence of Z_2 DPs, a pair of Fermi arcs with opposite chirality are found on the (100) surface of the PhC. The spectrum of such double Fermi arcs is mirror symmetric with respect to the $k_y = \pi/a$ line. The surface states are protected by the screw symmetry S_y which guarantees double degeneracy for $k_y = \pi/a$ in the surface BZ. Remarkably, parts of the surface states are below the light-line which hence allows realization of an "open cavity" on the PhC-air interface. We find that light is strongly confined around the interface due to the topological surface states, which allows *ultrastrong coupling* between TO-phonon in h-BN thin film and cavity photons. Such realization is feasible within current technology and has several fabrication and measurement advan-

tages. Our ultrastrong coupling system provides an emergent platform for the study of *extreme limits* in quantum optics and quantum phase transitions. With both strong interaction and nontrivial Berry phases, the system may host nontrivial states of matter such as strongly interacting bosonic topological states[7, 44]. Furthermore, TO-phonons in h-BN fall into the *mid infrared frequencies*, 170 meV, which is also important in manipulation of near field thermal emission[54, 55].

We also find that type-II Z_2 DPs have anomalous valley selective refraction: birefringence for one valley, while no refraction for the other. For the valley with birefringence, the two refraction beams have *opposite* refraction angles, one positive and the other negative. These findings open a window for the study of valley physics[56, 57] in Dirac and Weyl photonic systems.

Appendix A: $\vec{k} \cdot \vec{P}$ analysis of DPs

We use the $\vec{k} \cdot \vec{P}$ theory for photonic bands to study the low-energy Hamiltonian of the DPs. The photonic bands are solutions of the following eigenvalue equations

$$\boldsymbol{\nabla} \times \frac{1}{\varepsilon(\vec{r})} \boldsymbol{\nabla} \times \vec{h}_{n,\vec{k}}(\vec{r}) = \frac{\omega_{n,\vec{k}}^2}{c^2} \vec{h}_{n,\vec{k}}(\vec{r}), \qquad \text{(A1)}$$

where n is the band index and $\vec{h}_{n,\vec{k}}(\vec{r})$ is the Bloch function for the magnetic field of the electromagnetic wave. It is normalized as $\int_{u.c.} d\vec{r} \vec{h}_{n',\vec{k}}^*(\vec{r}) \vec{h}_{n,\vec{k}}(\vec{r}) = \delta_{nn'}$ with $u.c.$ denoting the unit cell (i.e., integration within a unit cell). The Hermitian operator $\boldsymbol{\nabla} \times \frac{1}{\varepsilon(\vec{r})} \boldsymbol{\nabla} \times$ is then regarded as the "photonic Hamiltonian"[30].

The $\vec{k} \cdot \vec{P}$ theory is constructed by expanding the Bloch functions of photonic bands near the DP with the Bloch functions at the DP. Direct calculation yields, the following $\vec{k} \cdot \vec{P}$ Hamiltonian,

$$\mathcal{H}_{nn'}(\vec{k}) = \frac{\omega_{n,0}^2}{c^2} \delta_{nn'} + \vec{q} \cdot \vec{P}_{nn'} - \int_{u.c.} \frac{d\vec{r}}{\varepsilon(\vec{r})} \vec{h}_{n,0}^*(\vec{r}) \cdot [\vec{q} \times (\vec{q} \times \vec{h}_{n',0}(\vec{r}))], \qquad \text{(A2)}$$

where $\omega_{n,0}$ is the eigen-frequency of the nth band at the DP. The matrix element of $\vec{P}$ is given by

$$\vec{P}_{nn'} = \int_{u.c.} \frac{d\vec{r}}{\varepsilon(\vec{r})} [\vec{h}_{n',0}(\vec{r}) \times (i\boldsymbol{\nabla} \times \vec{h}_{n,0}^*(\vec{r})) + (i\boldsymbol{\nabla} \times \vec{h}_{n',0}(\vec{r})) \times \vec{H}_{n,0}^*(\vec{r})]. \qquad \text{(A3)}$$

A crucial fact is that the matrix element $\vec{P}_{nn'}$ is nonzero only when the n and n' bands are of different parity. In our system the mirror planes are $y = x$, $y = -x$, and $z = 0.25$. Therefore, we shall calculate the two momentum matrix elements, $\hat{P}_1 = (\hat{P}_x + \hat{P}_y)/\sqrt{2}$ and $\hat{P}_2 = (-\hat{P}_x + \hat{P}_y)/\sqrt{2}$.

We calculate the $\vec{P}$ matrix element for the second DP at $k_z > 0$. The matrix form (band index goes from 3 to 6) gives (in arbitrary units),

$$\hat{P}_1 = \begin{pmatrix} 0 & 0 & 0 & 0 \\ 0 & 0 & -0.35 - 0.26i & -0.40 + 1.61i \\ 0 & -0.35 + 0.26i & 0 & 0 \\ 0 & -0.40 - 1.61i & 0 & 0 \end{pmatrix},$$

$$\hat{P}_2 = \begin{pmatrix} 0 & 0 & 1.65 + 0.04i & 0.16 + 0.4i \\ 0 & 0 & 0 & 0 \\ 1.65 - 0.04i & 0 & 0 & 0 \\ 0.16 - 0.4i & 0 & 0 & 0 \end{pmatrix}, \qquad \hat{P}_z = \begin{pmatrix} -0.74 & 0 & 0 & 0 \\ 0 & -0.74 & 0 & 0 \\ 0 & 0 & 1.5 & 0 \\ 0 & 0 & 0 & 1.5 \end{pmatrix}. \qquad \text{(A4)}$$

The $\vec{k} \cdot \vec{P}$ Hamiltonian in the $\vec{k}$ linear order is then

$$\hat{\mathcal{H}} - \frac{\omega_0^2}{c^2} \hat{1} \sim q_1 \hat{P}_1 + q_2 \hat{P}_2 + q_z \hat{P}_z, \qquad \text{(A5)}$$

where $q_1 = (q_x + q_y)/\sqrt{2}$ and $q_2 = (-q_x + q_y)/\sqrt{2}$, $q_x =$ $k_x - \pi/a$, $q_y = k_y - \pi/a$, and $q_z = k_z - k_{DP}$. The above Hamiltonian faithfully restore the symmetry and properties of the DP: (i) There are two doublets for each $\vec{q}$ [up to numerical error $\mathcal{O}(0.01)$]. (ii) Interaction is finite only between states of opposite parity. That is, the first
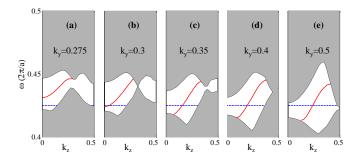
FIG. 9. (Color online) (a)-(e) Projected bulk bands (gray regions) and surface spectrum (red curves) vs. k_z for different k_y. All k_z and k_y are in units of $2\pi/a$. Frequencies are in unit of $\frac{2\pi c}{a}$. The blue line indicate the frequency $\omega = 0.425\frac{2\pi c}{a}$.
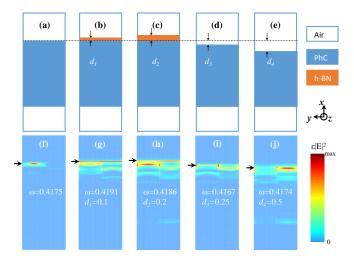

FIG. 10. (Color online) (a)-(e): Schematic of various modification of the supercell used in calculation of surface states. (a) Seven periods of PhC stacking along the x direction and $3a$ thick air layers above and below the PhC. (b) A layer of h-BN (thickness $0.1a$) is placed on top of the PhC. (c) A layer of h-BN of thickness $0.2a$ is placed on the top surface. (d) The top surface layer of PhC is cut by $0.25a$. (e) The top surface layer is cut by $0.5a$. (f)-(j): Frequency and energy profile $\varepsilon|\vec{E}|^2$ (integrated over z direction) in the x-y plane of the surface state with $\vec{k} = (0, 0.5, -0.3)\frac{2\pi}{a}$ for various situations. The arrows indicate the position of the top interface.

two states have opposite parity with the other two states.

Appendix B: Calculation of Fermi arcs associated with Z_2 DPs

To calculate the Fermi arcs on the (100) surface, we set a supercell with seven periods of PhC stacked along x direction. At the two sides of the PhC is an effective medium with $\varepsilon = 0.2$. This gives an effective refractive index $n = 0.45$ which promotes the light-line to higher frequency. This technique is to ensure all the surface

states of interest is confined to the surface. Without this treatment a portion of surface states is above light-line and are not confined to the surface any more. Similar skills have been employed to calculate the surface states on the (001) surface which are associated with Z_2 line-nodes.

We emphasize that the S_y symmetry is kept for our supercell computation by proper truncation of the structure [Similarly, the M_z symmetry is kept for the supercell calculation of (001) surface states]. The S_y symmetry is crucial in keeping the double degeneracy on the $k_y = \pi/a$ line in the surface BZ. The Fermi arcs are obtained by scanning the surface BZ. Specifically, for a series of k_y points, we calculate the projected bulk bands, as well as the spectrum of the surface states. The latter is obtained by comparing the spectrum of the supercell and the projected bulk bands. The states lie in the projected band gap are identified as the surface states. We show in Fig. 9 the spectrum of the projected bulk bands (gray) and surface states (red). The Fermi arc is obtained via finding the $\vec{k}$ points in the surface BZ with the given frequency (i.e., the intersection between the red curve and the blue line). The spectrum is symmetric for positive and negative k_y (or k_z), hence we only need to compute a quarter of the surface BZ. We remark that from Figs. 9(a) and 9(b), one can infer that the Fermi arcs at $k_z > 0$ and $k_z < 0$ are continuously connected. In contrast, since the intersection between the blue line and surface state spectrum is protected by topology at $k_y = \pi/a$ [the edge spectrum traversing the "valence" and "conduction" bands as shown in Fig. 9(e)], the intersection of Fermi arcs with $k_y = \pi/a$ line is protected. Hence, the $k_y = \pi/a$ line separates the two Fermi arcs, which is consistent with bulk-edge correspondence principle.

Appendix C: Robustness of topological states on (100) surface

To demonstrate the robustness of the topological surface states for (100) surface associated Z_2 DPs, we calculate the frequency and field profiles for various modification of the supercell. The supercell, as demonstrated in Fig. 10(a) consists of seven periods of our PhC and air regions of thickness $3a$ above and below the PhC. The structure is staked along x direction. There are two PhC-air interfaces, we only focus on one of them (the top surface shown in Fig. 10). Beside such a supercell, we also calculate the following four situations (all for the wavevector $\vec{k} = (0, 0.5, -0.3)\frac{2\pi}{a}$ which is below the light-line): (1) When a h-BN layer of thickness $d_1 = 0.1a$ is placed on top of the PhC. The dielectric constant of the h-BN is taken as $\varepsilon_{BN} = 8$ as from experiments[52]. (2) When the thickness of the h-BN layer is $d_2 = 0.2a$. (3) When the surface layer is cut by $d_3 = 0.25a$. (4) When the surface layer is cut by $d_4 = 0.5a$. The geometries for those modifications are illustrated in Figs. 10(b)-(e). For all the situations, the bottom surface is left un-

changed. The frequency of the surface state as well as its energy distribution for various situations are shown in Figs. 10(f)-(j). It is seen that the frequency of the surface state changes negligibly for various situations, although the energy distribution has been modified. These results demonstrate the robustness of the topological surface states.

[1] M. Z. Hasan and C. L. Kane, *Topological Insulators*, Rev. Mod. Phys. **82**, 3045 (2010).

[2] X.-L. Qi and S.-C. Zhang, *Topological insulators and superconductors*, Rev. Mod. Phys. **83**, 1057 (2011).

[3] O. Vafek and A. Vishwanath, *Dirac Fermions in Solids: From High-Tc Cuprates and Graphene to Topological Insulators and Weyl Semimetals*, Ann. Rev. Cond. Matt. Phys. **5**, 83 (2014).

[4] Y. Chen, Y.-M. Lu, and H.-Y. Kee, *Topological Crystalline Metal in Orthorhombic Perovskite Iridates*, Nat. Commun. **6**, 6593 (2015).

[5] Y. Chen, H.-S. Kim, and H.-Y. Kee, *Topological crystalline semimetals in non-symmorphic lattices*, Phys. Rev. B **93**, 155140 (2016).

[6] X. G. Wen, *Quantum Field Theory of Many-Body Systems* (Oxford University Press, Oxford, 2004).

[7] X. Chen, Z.-C. Gu, Z.-X. Liu, and X.-G. Wen, *Symmetry Protected Topological Orders in Interacting Bosonic Systems*, Science **338**, 1604-1606 (2012).

[8] Z. Wang, Y. Sun, X.-Q. Chen, C. Franchini, G. Xu, H. Weng, X. Dai, and Z. Fang, *Dirac semimetal and topological phase transitions in A_3Bi (A=Na, K, Rb)*, Phys. Rev. B **85**, 195320 (2012).

[9] Z. K. Liu, B. Zhou, Y. Zhang, Z. J. Wang, H. M. Weng, D. Prabhakaran, S.-K. Mo, Z. X. Shen, Z. Fang, X. Dai, Z. Hussain, and Y. L. Chen, *Discovery of a Three-Dimensional Topological Dirac Semimetal, Na_3Bi*, Science **343**, 864 (2014).

[10] T. Liang, Q. Gibson, M. N. Ali, M. Liu, R. J. Cava, and N. P. Ong, *Ultrahigh mobility and giant magnetoresistance in the Dirac semimetal Cd_3As_2*, Nat. Mater. **14**, 280 (2015).

[11] L. Lu, Z. Wang, D. Ye, L. Ran, L. Fu, J. D. Joannopoulos, and M. Soljačić, *Experimental observation of Weyl points*, Science **349**, 622 (2015).

[12] S.-Y. Xu, I. Belopolski, N. Alidoust, M. Neupane, G. Bian, C. Zhang, R. Sankar, G. Chang, Z. Yuan, C.-C. Lee, S.-M. Huang, H. Zheng, J. Ma, D. S. Sanchez, B.K. Wang, A. Bansil, F. Chou, P. P. Shibayev, H. Lin, S. Jia, and M. Z. Hasan, *Discovery of a Weyl fermion semimetal and topological Fermi arcs*, Science **349**, 613 (2015).

[13] B.Q. Lv, H.M. Weng, B.B. Fu, X.P. Wang, H. Miao, J. Ma, P. Richard, X.C. Huang, L.X. Zhao, G.F. Chen, Z. Fang, X. Dai, T. Qian, and H. Ding, *Experimental Discovery of Weyl Semimetal TaAs*, Phys. Rev. X **5**, 031013 (2015).

[14] A. Chutinan, S. John, and O. Toader, *Diffractionless Flow of Light in All-Optical Micro-chips*, Phys. Rev. Lett. **90**, 123901 (2003).

[15] F. D. M. Haldane and S. Raghu, *Possible realization of directional optical waveguides in photonic crystals with broken time-reversal symmetry*, Phys. Rev. Lett. **100**, 013904 (2008).

[16] Z. Wang, Y. D. Chong, J. D. Joannopoulos, and M. Soljačić, *Reflection-free one-way edge modes in a gyromagnetic photonic crystal*, Phys. Rev. Lett. **100**, 013905 (2008).

[17] M. Hafezi, E. A. Demler, M. D. Lukin, J. M. Taylor, *Robust optical delay lines with topological protection*, Nat. Phys. **7**, 907 (2011).

[18] I. Söllner, S. Mahmoodian, S. L. Hansen, L. Midolo, A. Javadi, G. Kiršanské, T. Pregnolato, H. El-Ella, E. Hye Lee, J. D. Song, S. Stobbe, and P. Lodahl, *Deterministic photon-emitter coupling in chiral photonic circuits*, Nat. Nanotech. **10**, 775 (2015).

[19] M. D. Turner, M. Saba, Q. Zhang, B. P. Cumming, G. E. Schröder-Turk, and M. Gu, *Miniature chiral beamsplitter based on gyroid photonic crystals*, Nat. Photon. **7**, 801 (2013).

[20] Z. Wang, Y. Chong, J. D. Joannopoulos, and M. Soljačić, *Observation of unidirectional backscattering-immune topological electromagnetic states*, Nature (London) **461**, 772 (2009).

[21] K. Fang, Z. Yu, and S. Fan, *Realizing effective magnetic field for photons by controlling the phase of dynamic modulation*, Nat. Photon. **6**, 782 (2012).

[22] M. Hafezi, S. Mittal, J. Fan, A. Migdall, and J. Taylor, *Imaging topological edge states in silicon photonics*, Nat. Photon. **7**, 1001 (2013).

[23] L. Lu, L. Fu, J. D. Joannopoulos, and M. Soljačić, *Weyl points and line nodes in gyroid photonic crystals*, Nat. Photon. **7**, 294 (2013).

[24] M. C. Rechtsman, J. M. Zeuner, Y. Plotnik, Y. Lumer, D. Podolsky, F. Dreisow, S. Nolte, M. Segev, and A. Szameit, *Photonic Floquet topological insulators*, Nature **496**, 196 (2013).

[25] X. Huang, Y. Lai, Z. H. Hang, H. Zheng, and C. T. Chan, *Dirac cones induced by accidental degeneracy in photonic crystals and zero-refractive-index materials*, Nat. Mater. **10**, 582 (2011).

[26] A. B. Khanikaev, S. H. Mousavi, W.-K. Tse, M. Kargarian, A. H. MacDonald, and G. Shvets, *Photonic topological insulators*, Nat. Mater. **12**, 233 (2013).

[27] W.-J. Chen, S.-J. Jiang, X.-D. Chen, J.-W. Dong, and C. T. Chan, *Experimental realization of photonic topological insulator in a uniaxial metacrystal waveguide*, Nat. Commun. **5**, 5782 (2014).

[28] L.-H. Wu and X. Hu, *Scheme for Achieving a Topological Photonic Crystal by Using Dielectric Material*, Phys. Rev. Lett. **114**, 223901 (2015).

[29] C. He, X.-C. Sun, X.-P. Liu, M.-H. Lu, Y. Chen, L. Feng, and Y.-F. Chen, *Photonic topological insulator with broken time-reversal symmetry*, Proc. Natl. Acad. Sci. USA **113**, 4924 (2016).

[30] H.-X. Wang, L. Xu, H.-Y. Chen, and J.-H. Jiang, *Three-dimensional photonic Dirac points stabilized by point group symmetry*, Phys. Rev. B **93**, 235155 (2016).

[31] W. Gao, B. Yang, M. Lawrence, F. Fang, B. Béri, and S. Zhang, *Plasmon Weyl Degeneracies in Magnetized Plasma*, arXiv:1511.04875

[32] L. Lu, J. D. Joannopoulos, and M. Soljačić, *Topological photonics*, Nat. Photon. **8**, 821 (2014).

[33] M. Xiao, Z. Q. Zhang, and C. T. Chan, *Surface Impedance and Bulk Band Geometric Phases in One-Dimensional Systems*, Phys. Rev. X **4**, 021017 (2014).

[34] W.-J. Chen, M. Xiao, and C. T. Chan, *Experimental observation of robust surface states on photonic crystals possessing single and double Weyl points*, arXiv:1512.04681

[35] M. Hafezi, *Measuring Topological Invariants in Photonic Systems*, Phys. Rev. Lett. **112**, 210405 (2014).

[36] S. Mittal, S. Ganeshan, J. Fan, A. Vaezi, and M. Hafezi, *Measurement of topological invariants in a 2D photonic system*, Nat. Photon. **10**, 180 (2016).

[37] L. Lu, C. Fang, L. Fu, S. G. Johnson, J. D. Joannopoulos, and M. Soljačić, *Symmetry-stabilized topological photonic crystal in three dimensions*, Nat. Phys. **12**, 337 (2016).

[38] I. Carusotto and C. Ciuti, *Quantum fluids of light*, Rev. Mod. Phys. **85**, 299 (2013).

[39] T. Niemczyk, F. Deppe, H. Huebl, E. P. Menzel, F. Hocke, M. J. Schwarz, J. J. Garcia-Ripoll, D. Zueco, T. Hümmer, E. Solano, A. Marx, and R. Gross, *Circuit quantum electrodynamics in the ultrastrong-coupling regime*, Nat. Phys. **6**, 772 (2010).

[40] Y. Todorov, A. M. Andrews, R. Colombelli, S. De Liberato, C. Ciuti, P. Klang, G. Strasser, and C. Sirtori, *Ultrastrong Light-Matter Coupling Regime with Polariton Dots*, Phys. Rev. Lett. **105**, 196402 (2010).

[41] G. Scalari, C. Maissen, D. Turčinková, D. Hagenmüller, S. De Liberato, C. Ciuti, C. Reichl, D. Schuh, W. Wegscheider, M. Beck, and J. Faist, *Ultrastrong Coupling of the Cyclotron Transition of a 2D Electron Gas to a THz Metamaterial*, Science **335**, 1323 (2012).

[42] G. Günter, A. A. Anappara, J. Hees, A. Sell, G. Biasiol, L. Sorba, S. De Liberato, C. Ciuti, A. Tredicucci, A. Leitenstorfer, and R. Huber, *Sub-cycle switch-on of ultrastrong lightmatter interaction*, Nature 458, 178 (2009).

[43] S. De Liberato, C. Ciuti, and I. Carusotto, *Quantum Vacuum Radiation Spectra from a Semiconductor Microcavity with a Time-Modulated Vacuum Rabi Frequency*, Phys. Rev. Lett. **98**, 103602 (2007).

[44] E. Kapit, M. Hafezi, and S. H. Simon, *Induced Self-Stabilization in Fractional Quantum Hall States of Light*, Phys. Rev. X **4**, 031039 (2014).

[45] http://abinitio.mit.edu/wiki/index.php/MITPhotonicBands.

[46] B.-J. Yang, T. Morimoto, and A. Furusaki, *Topological charges of three-dimensional Dirac semimetals with rotation symmetry*, Phys. Rev. B **92**, 165120 (2015).

[47] J.-H. Jiang, *Tunable topological Weyl semimetal from simple-cubic lattices with staggered fluxes*, Phys. Rev. A **85**, 033640 (2012).

[48] C. Fang, L. Lu, J. Liu, and L. Fu, *Topological semimetals with helicoid surface states*, arXiv:1512.01552, Nat. Phys. in press.

[49] C. Fang, Y. Chen, H.-Y. Kee, and L. Fu, *Topological nodal line semimetals with and without spin-orbital coupling*, Phys. Rev. B **92**, 081201 (2015)

[50] J.-H. Jiang and S. John, *Photonic Crystal Architecture for Room-Temperature Equilibrium Bose-Einstein Condensation of Exciton Polaritons*, Phys. Rev. X **4**, 031025 (2014).

[51] J.-H. Jiang and S. John, *Photonic Architectures for Equilibrium High-Temperature Bose-Einstein Condensation in Dichalcogenide Monolayers*, Sci. Rep. 4, 7432 (2014).

[52] R. Geick, C. H. Perry, and G. Rupprecht, *Normal Modes in Hexagonal Boron Nitride*, Phys. Rev. **146**, 543 (1966).

[53] A. Ridolfo, M. Leib, S. Savasta, and M. J. Hartmann, *Photon Blockade in the Ultrastrong Coupling Regime*, Phys. Rev. Lett. **109**, 193602 (2012).

[54] Y. Guo, C. L. Cortes, S. Molesky, and Z. Jacob, *Broadband super-Planckian thermal emission from hyperbolic metamaterials*, Appl. Phys. Lett. **101**, 131106 (2012).

[55] S.-A. Biehs, M. Tschikin, R. Messina, and P. Ben-Abdallah, *Super-Planckian near-field thermal emission with phonon-polaritonic hyperbolic metamaterials*, Appl. Phys. Lett. **102**, 131106 (2013).

[56] K. F. Mak, K. He, J. Shan, and T. F. Heinz, *Control of valley polarization in monolayer MoS_2 by optical helicity*, Nat. Nanotech. **7**, 494 (2012).

[57] Q.-D. Jiang, H. Jiang, H. Liu, Q.-F. Sun, and X. C. Xie, *Topological Imbert-Fedorov shift in Weyl semimetals*, Phys. Rev. Lett. **115**, 156602 (2015).